Mechanical Systems and Signal Processing 118 (2019) 696–715

Contents lists available at ScienceDirect

Mechanical Systems and Signal Processing

journal homepage: www.elsevier.com/locate/ymssp

Identification of multi-dimensional elastic and dissipative properties of elastomeric vibration isolators

Ram S. Ramesh, Luke Fredette, Rajendra Singh *

Acoustics and Dynamics Laboratory, NSF Smart Vehicle Concepts Center, Department of Mechanical and Aerospace Engineering, The Ohio State University, Columbus, OH 43210, USA

ARTICLE INFO

Article history:
Received 9 January 2018
Received in revised form 1 June 2018
Accepted 3 September 2018
Available online 15 September 2018

Keywords:
System identification
Experimental characterization
Modal methods
Stiffness coupling
Rigid body isolation

ABSTRACT

Experimental methods must be adopted to characterize the dynamic properties of elastomeric isolators, especially their multi-dimension elastic and dissipative properties. To facilitate a tractable problem statement a rigid body isolation system (under a weight-type preload) is proposed and reduced to a planar problem with 3 degrees of freedom that can be replicated in any vertical plane. First, this article employs modal methods in tandem with analytical, lumped-parameter models to experimentally characterize the dynamic stiffness matrix, including off-diagonal terms. Fundamental stiffness properties are identified about the elastic center, facilitating a clear relationship between component- and system-level dynamics. Dissipative properties are analyzed in terms of global, structural type and mode-dependent viscous type damping formulations. Modal decomposition is employed to demonstrate the effectiveness of the dissipative models for both coupled and uncoupled motions. The proposed characterization method is validated by comparing predicted dynamic properties of a multi-isolator system with measured responses in multiple directions. Finally, physical insight into the underlying behavior of elastomeric interfacial elements is sought by highlighting the role of the elastic center, comparing structural loss factor and viscous damping matrix models, identifying the correlation between surface hardness and Young's Modulus, and briefly comparing non-resonant and resonant methods. Several annular or cylindrical elastomeric devices with varying size and material demonstrate the proposed method's breadth of application; subsequently, two production mounts are utilized for validation purposes. Various identification issues such as uniqueness of the identified stiffness, damping and elastic center properties are discussed throughout the article.

© 2018 Elsevier Ltd. All rights reserved.

1. Introduction

Natural and synthetic elastomeric materials are employed for a broad range of vibration isolation systems. Such devices exhibit amplitude and frequency dependent stiffness and damping properties which pose difficulties in the dynamic characterization. Furthermore, these materials are often sensitive to manufacturing processes, and may be non-homogenous and anisotropic; therefore, experimental methods must be adopted [1].

* Corresponding author.
E-mail address: singh.3@osu.edu (R. Singh).

https://doi.org/10.1016/j.ymssp.2018.09.009
0888-3270/© 2018 Elsevier Ltd. All rights reserved.

Methods of characterizing the dynamic properties of elastomeric isolators may be broadly categorized into resonant or non-resonant approaches. Non-resonant methods typically use uniaxial, sinusoidal excitation using an electro-hydraulic system [2–7] or electro-dynamic shaker [8–11]. This method applies the dynamic displacement while the specimen is under a mean load, and the force transmitted to the rigid base is analyzed at the excitation frequency to yield the dynamic stiffness of the device. With a visco-elastic model, the stiffness modulus and loss factor may be mapped over a range of frequencies, amplitudes, and mean loads. However, only diagonal stiffness matrix elements (such as compression and shear) may be measured in this manner, and isolator fixtures are often required which may introduce additional dynamics that distort some results.

Resonant (modal) methods generally rely on a system perspective and thus isolators are in a mechanical or structural system, and dynamic mobilities are measured using impulse hammer or shaker tests. The component-level property is then inferred from the system-level vibration response [10–13]. For example, Lin et al. [10] and Ooi et al. [11] characterized the vertical dynamic stiffness of an isolator in a simple uniaxial system using the frequency response from an impulse hammer test and validated their results through comparison with a non-resonant test. However, neither took into account additional degrees of freedom. Kim and Singh [12] placed the isolator between two compact, identical masses and conducted cross-point measurements, using a mobility method to indirectly identify the multi-axis stiffness of the interfacial element, but no mean load was applied in their experiments. Meggitt et al. [13] used a procedure similar to Kim and Singh's, and extended the mobility method to include an isolator placed between two flexible elements to simulate an *in situ* measurement. While both studies showed reasonable accuracy over a wide range of frequencies and considered several isolator geometries, the mobility method is inherently prone to the accumulation of numerical error since the solution is found through matrix inversion. Noll et al. [4] investigated the relationship between the dynamics of an isolated elastic beam structure and the isolator stiffness matrix of dimension 3, including limited off-diagonal terms. A modal approach (but without a mean load) was taken to analyze the system, and the inferred isolator stiffness values were validated by non-resonant measurements. The importance of system-component interactions is highlighted by [4], suggesting that proper characterization of boundary conditions is critical for any indirect characterization method. Further, Joodi et al. [5] have shown the numerical errors that can result from such an indirect method. Finally, while resonant and non-resonant methods are distinct, elements of each may be combined to form a hybrid procedure. For instance, Thompson et al. used a non-resonant measurement, but focused on the resonance behavior of the resulting frequency response functions to indirectly identify the uniaxial stiffness of a rail pad [9].

The concept of elastic center has occasionally been used in the study of mechanical systems [14,15], but to the authors' knowledge, the utility of this physical characteristic has not been applied in the identification of elastomeric interfacial devices. The center of elasticity is a location about which pure translational forces yield pure displacements and pure moments produce rotations only; in short, the component stiffness matrix will be diagonal if and only if the coordinate system's origin is coincident with the elastic center. Locating this point offers great clarity vis-à-vis off-diagonal stiffness terms since these depend on the coordinate system. This article seeks to develop a simplified, experimental identification procedure based on locating and using the elastic center for interfacial connections. The proposed modal analysis based approach, while relying on key knowledge elements from prior literature, aims to offer multi-axis dynamic stiffness (including off-diagonal terms) and damping characterization, as well as insights into component and isolation system level behavior.

2. Problem formulation

To facilitate a tractable problem statement, the full 6 degree of freedom isolation system is reduced to a planar, 3 degree of freedom problem that can be replicated in any vertical plane. A modal approach is employed with a frequency range of interest up to 200 Hz. Several annular or cylindrical elastomeric devices with geometry depicted in Fig. 1(a) and with different sizes and materials demonstrate the proposed method's breadth of application. Subsequently, several production mounts

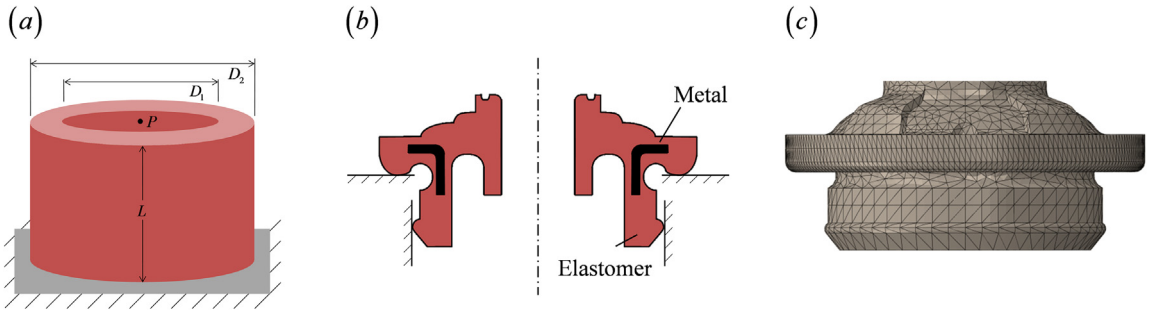

Fig. 1. Geometry of (*a*) laboratory isolators, (*b*) production isolator V, and (c) the finite element model of the isolator V. Here, L is the length, D_1 is the inner diameter, and D_2 is the outer diameter of the lab isolators, and P is the central point of the mating surface in (*a*), representing the location of physical connection to the supported structure.

as shown in Fig. 1(b) are utilized for validation purposes. The designation and physical parameters of each laboratory isolator are given in Table 1. The production mounts (designated V) are comprised of ethylene propylene diene monomer rubber (EPDM) and are evaluated for a Shore A hardness (*S*, ASTM: D2240) of 41, 49, 59, and 68. Isolator V also contains a metal insert as seen in Fig. 1(b). Three experimental configurations as displayed in Fig. 2 are employed for identification and validation. In test configuration *T-A*, a single isolator supports a 0.7 kg mass on a grounded plate, and modal tests are undertaken for system characterization. Test configuration *T-B* has a 12.4 kg thick steel plate supported by four identical isolators near the corners. This setup serves as experimental validation, where the system dynamics are compared with predictions made by using the component stiffness matrix from configuration *T-A*. Finally, test configuration *T-C* serves as a more realistic validation by combining two pairs of dissimilar production mounts in a physical system that mimics the *in situ* isolation application. In this case, a vertically oriented, 6.7 kg thick steel plate is placed on two relatively stiff isolators with much more compliant mounts near the top of the plate, constraining out-of-plane motion. Each configuration's mass is selected to provide appropriate pre-load, stability, and dynamic scaling. The mass provides the only source of pre-load, so it must be tuned to achieve a reasonable operating point and ensure linear system type behavior. For stability, it must also be light enough so that small placement eccentricities do not tend to make the experiment tip over. To provide appropriate dynamic scaling, the geometry of the mass is selected to (together with the combined mount stiffness properties) keep the natural frequency sequence and values similar to the *in situ* application.

The objectives of this article are to (1) experimentally characterize the dynamic stiffness matrix (including off-diagonal terms) and damping properties of a compliant elastomeric mount with particular focus on the center of elasticity, (2) experimentally validate the characterization method by comparing predicted dynamic properties of a multi-isolator system with measurements, and (3) obtain physical insight into the underlying behavior of elastomeric interfacial elements by highlighting the role of the elastic center, comparing damping models, and identifying the correlation between surface hardness *S* and Young's Modulus *E*. Analytical (lumped-parameter) models will be used to guide the experimental work, and computational, finite element models will be employed alongside these in both the identification and validation steps. Unlike some prior methods, this work utilizes modal methods with rigid body isolation to limit the number of modes in consideration and to achieve good coupling between multi-dimensional motions. This should allow the isolator properties to be extracted from system-level measurements, with the intent to achieve demonstrably unique solutions. The unique solution approach should also circumvent the numerical conditioning problems which are inherent to frequency response function based methods [5,12]. Both structural and viscous damping models will be considered to capture the global or mode-dependent dissipative behavior of various materials.

Since the focus of this article is the multi-axis, dynamic, elastic and dissipative characterization of elastomeric isolators, many other factors must be ignored to facilitate a tractable problem. These include hyperelasticity, thermal effects, and material damage or aging. Inclusion of these factors into the proposed identification procedures is thus left to future work.

The scope of this study is thus limited to linear time-invariant system theory, which assumes small displacements about an operating point; this is consistent with prior mobility methods [12,13]. The associated mass-loading of additional preload may be easily accounted for in the model, so the proposed identification method may be applied under various pre-loads as long as the operating point is in a relatively linear regime of the force deflection curve. Force deflection curves for isolators I-IV are shown in Fig. 3, demonstrating nearly linear stiffness regimes over significant ranges of displacement. However, a treatment of amplitude or frequency dependence (typical of non-resonant methods [5,6]) is beyond the scope of this work. Real-valued eigenvalue analysis is used throughout this article, so estimation of damping properties is treated separately from the stiffness identification; complex eigensolutions are left to future work.

3. Procedure for identifying elastic properties

3.1. Determination of elastic center

To locate the elastic center, *O*, of an isolator, a finite element model of the device is employed (as seen in Fig. 1(c) for Isolator V, for the sake of illustration). Estimated values of *E* may be obtained from *S* using the empirical relations proposed in [16], while other properties such as ρ and ν may be assumed directly based on the material composition. Interfacial surfaces are selected based on the mounting configuration of the isolator, and all nodes on each surface are kinematically linked. In the case of the laboratory isolators I to IV, the top and bottom surfaces are selected, and the bottom surface is given a fixed boundary condition. Next, two points, *P* and *Q*, are defined forming a vector which is coincident with the specified hard point

Table 1
Geometric parameters and material properties of laboratory isolators in Fig. 1(a).

Isolator Designation	Material	L (mm)	D_1 (mm)	D_2 (mm)	S	ν	ρ (kg/m^3)	ε_z (mm)
I	Polyurethane	33.6	38.1	51.3	40	0.49	1252	16.8
II	Polyurethane	35.3	38.1	50.9	60	0.49	1266	17.6
III	Silicone	34.3	23.6	38.1	60	0.49	1535	17.1
IV	EPDM	30.7	0	49.8	60	0.49	1187	15.3

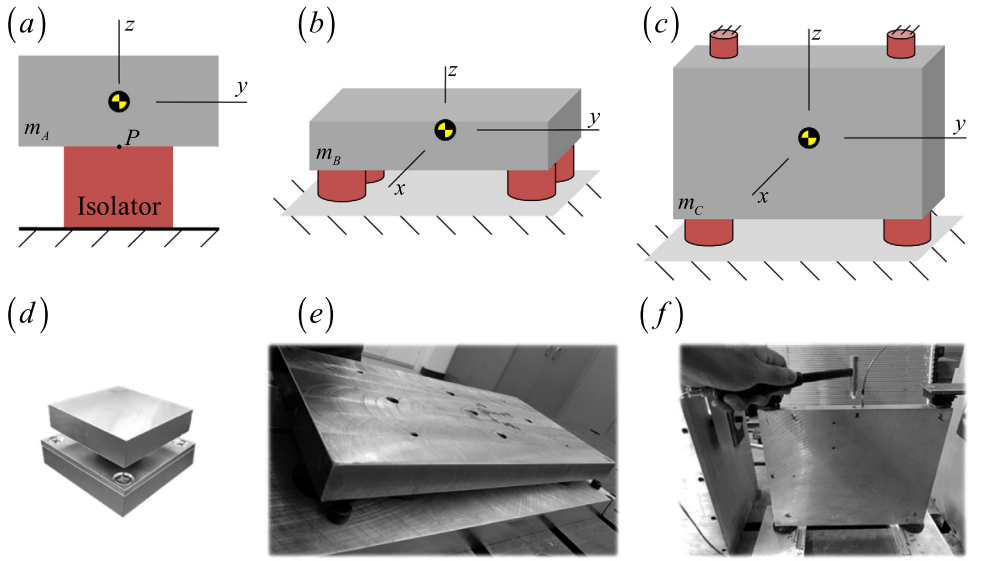

Fig. 2. System configurations used for experimental identification and validation: (*a*) single-mount configuration *T-A* used to characterize an isolator; (*b*) 4-mount horizontal configuration *T-B* is used to validate laboratory isolators I to IV, and (*c*) 4-mount vertical configuration *T-C* utilizes two pairs of dissimilar, production isolators to mimic *in situ* application and provide more realistic validation. Photographs are also given for configurations (*d*) *T-A*, (*e*) *T-B*, and (*f*) *T-C*. Here, m_A, m_B, and m_C represent the mass of the inertial element in each configuration.

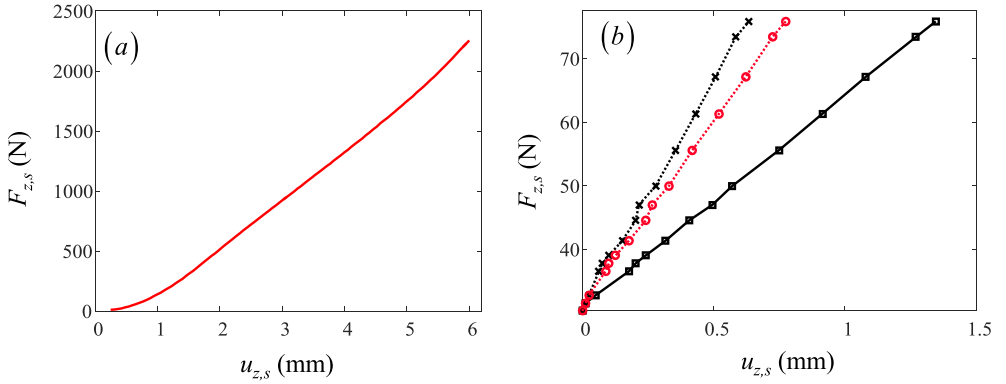

Fig. 3. Measured static load–deflection curve in the axial (*z*) direction for (*a*) isolator IV, measured by a dynamic elastomer test machine [2] over a wide range of mean loads and (*b*) isolators I, II and III from static displacements (under known weights) over a narrow range of mean loads. A nearly linear stiffness regime is found in all cases. Key: —■— – Isolator I; ···×··· – Isolator II; ···○··· – Isolator III; —— – Isolator IV. Here, $F_{z,s}$ is the static load acting on the isolator in the *z* direction and $u_{z,s}$ is the static, translational displacement in the *z* direction.

(*P*) and collinear with the geometric central axis of the mount as shown in Fig. 4(a)—the length of *PQ* is unimportant. The distance between *O* and *P* in each direction is defined as ε_x, ε_y, and ε_z. A moment is applied about an axis perpendicular to *PQ* (the positive *x*-axis in this case), which moves *PQ* to *P′Q′*. Since a pure moment was applied, *O* will be the center of rotation for this displacement, and may be located by finding the intersection of the perpendicular bisectors of *PP′* and *QQ′* using a vector loop. However, this method is very sensitive to changes in the length of *PQ*, so some conditioning is necessary in practice to avoid significant numerical error. For symmetric isolators, the assumption that *O* lies on the axis of symmetry ($\varepsilon_x = \varepsilon_y = 0$) indeed simplifies the procedure, as shown in Fig. 4(b). In this case, *O* is also located at the intersection of *PQ* and *P′Q′*, and the calculation procedure is much less sensitive to small numerical errors. The resulting value of ε_z for each laboratory isolator is given in Table 1. The values are found to be close to $L/2$ where *L* is the length of the annular or cylindrical isolator.

The proposed procedure could be reproduced physically to measure the location of *O*, but precise static or dynamic forces/moments and multi-dimensional motion measurements would be required at multiple locations, turning a relatively simple computational procedure into a potentially impractical experiment. All analytical models in this article are dependent

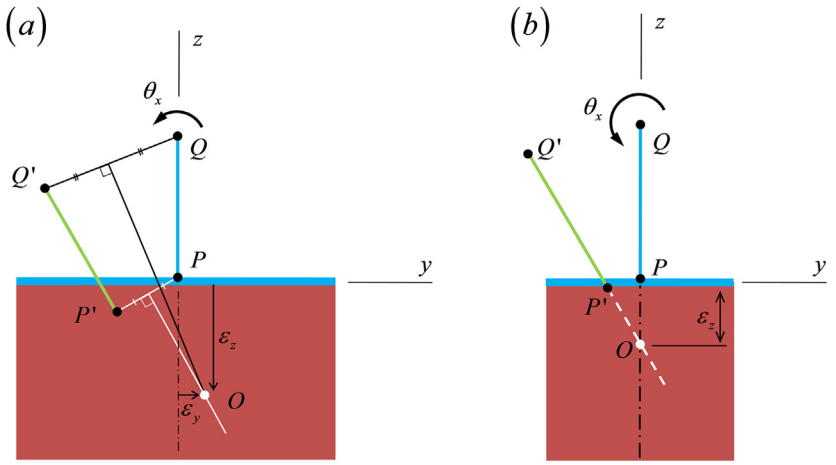

Fig. 4. Elastic center geometry (*a*) for the general planar problem and (*b*) assuming that *O* lies on the central axis. Here, PQ is collinear with the isolator's geometric central axis and kinematically linked to the contact surface while P′Q′ is the deformed location of PQ under a purely rotational load which is orthogonal to PQ. In general, the elastic center lies on the intersection of the perpendicular bisectors of PP′ and QQ′; however, if the elastic center resides on the central axis of the isolator, then it will also lie on the intersection of PQ and P′Q′.

on accurate knowledge of the *O* location; therefore, these calculations are implicitly validated by the modal experiments discussed hereafter.

3.2. Modal experiments

Configuration *T-A* is employed first to characterize the stiffness matrix of each mount. These include the laboratory isolators I through IV (with properties given in Table 1), and a production isolator V with *S* values of 41, 49, 59, and 68. Although this configuration is relatively robust to characterize a wide array of different vibration isolator designs and materials, it is limited by its relative instability under a large preload (especially for mounts with lower *S*). A more robust discussion of preload issues will be given later; nevertheless, under limited preload, both driving-point and cross-point accelerance measurements may be taken in multiple directions to fully capture six rigid body modes of the system.

To guide the experimental procedure, a finite element model similar to the one shown in Fig. 1(c) is first analyzed to identify the six natural frequencies and modeshapes of the system corresponding to rigid body motion of the inertial element. Although dependent on the estimated value of *E*, these demonstrate appropriate excitation and sensor locations and estimate the necessary frequency resolution and range. The applied force and acceleration measurements are taken, averaged in the frequency domain, and then used to obtain particular driving- and cross-point accelerance terms, $\tilde{A}(\omega)$, which are useful to identify the natural frequencies, ω_n. Here, the tilde represents a complex-valued quantity. Specifically, a driving point measurement is taken with the excitation force (F_Z) acting at the center of the top surface of the mass, such that the force's line of action passes through the CG, yielding $\tilde{A}_{zz}(\omega) = -\omega^2 u_z/F_z|_\omega$, where ω is the frequency in rad/s and u_z is the displacement of the mass in *z* direction. Similarly, a second measurement is taken laterally such that the line of action passes through the CG and on to the accelerometer yielding $\tilde{A}_{yy}(\omega) = -\omega^2 u_y/F_y|_\omega$ for a coordinate system centered at the CG. As expected, each experimental configuration has one uncoupled bounce mode along the *z* direction, one uncoupled torsional mode along θ_z, coupled shear and rocking modes along the *y* and θ_x directions respectively, and another pair of coupled shear and rocking modes along the *x* and θ_y directions respectively. Due to the geometric symmetry of configuration *T-A*, excitations in the *x* and *y* directions yield identical results (indicating symmetric modes, i.e. ω_2=ω_3 and ω_4=ω_5), so only the results for excitation in the *y* and *z* directions are given. The true natural frequencies of the system are estimated from the measured accelerance magnitude $\left|\tilde{A}(\omega)\right|$ spectra, $\{\omega_n\} = \{18\text{ Hz},\ 46\text{ Hz},\ 64\text{ Hz}\}$ for Isolator I, corresponding to the shear, rocking, and bounce modes, respectively. The natural frequencies for Isolators II and III are $\{\omega_n\} = \{26\text{ Hz},\ 65\text{ Hz},\ 90\text{ Hz}\}$ and $\{\omega_n\} = \{23\text{ Hz},\ 67\text{ Hz},\ 98\text{ Hz}\}$, in the same order. More details on the estimation procedure are given in Section 5. These may be used to update the value of *E* in the finite element model if needed.

The instrumentation used for modal measurements includes an accelerometer (PCB model A353B66), impulse hammer (PCB model 086C03), single module carrier (NI USB-9162) and vibration input module (NI, model 9234) for the data acquisition system. The post-processing is performed using NI LabVIEW SignalExpress and MATLAB. A sampling frequency of 1000 Hz with a frequency resolution of 0.8 Hz is used for signal processing, and three samples at each location are averaged to minimize the random error in the accelerance measurements (with root-mean-square averaging in frequency domain).

3.3. Development of analytical models

The full 6 degree-of-freedom (DOF) problem for configuration *T-A* is reduced to a more tractable 3 mode problem by ensuring that planes of symmetry may be defined containing both the elastic center and the center of mass. A 3-DOF analytical model can then be used to describe the behavior of the system in any of these planes independently. For simplicity, only one such vertical plane (*y-z*) is considered in this section. Since the torsional mode is uncoupled, a single degree of freedom system could be defined for the θ_z direction, although this is trivial and thus not developed here. In this manner, the complete stiffness matrix of dimension 6 can be constructed about the elastic center *O* using this analytical framework.

To identify the stiffness property and ensure that the analytical model has similar dynamic behavior to the physical device, three steps are performed: (i) analytically relate the eigensolution to the stiffness matrix about *O* ($[K]_O$) which may be considered the fundamental stiffness property of the device, (ii) populate $[K]_O$ from the measured natural frequencies, and (iii) verify the analytical model for configuration *T-A* in terms of the eigensolution using the finite element model. Additionally, such analytical models may aid in the interpretation of the experimental measurements and computational exercises.

The 3-DOF analytical model used in this study is depicted in Fig. 5. The stiffness matrix about *O* is, by definition, a diagonal matrix, but for coordinate systems located another point (such as the "hard point" *P* or center of gravity (CG) G of the mass) the matrix will contain off-diagonal terms. Both $\varepsilon_y, \varepsilon_z \neq 0$ are allowed in the model for generality, and the distance from *P* to G is given by *a*. Three distinct springs, k_y, k_z, and k_θ support *O* from the ground in the *y*, *z*, and rotational directions, respectively, corresponding to diagonal $[K]_O$. Since a rigid kinematic link between *O* and *P* rigidly attaches the mass, all stiffness elements are considered to be acting at *O*. The governing equation for the undamped system displayed in Fig. 5(a) (from the static equilibrium under a given preload) is given below where the generalized displacement vector $\{q(t)\} = \{u_y(t), u_z(t), \theta_x(t)\}^T$ is given in a right-handed coordinate system center at G, $\{F(t)\}$ is the dynamic (external) force vector, $[M] = diag[m_A, m_A, J_{xxA}]$ is the mass matrix, and $[K]_G$ is the system stiffness matrix about G:

$$[M]\{\ddot{q}(t)\} + [K_G]\{q(t)\} = \{F(t)\}. \tag{1}$$

Here, $[K]_G$ is related to $[K]_O$ through kinematic transformation. Fig. 5(b) depicts a generalized rigid body where $\{R\} = \{R_y, R_z\}$ is a vector from the CG to an attachment point (*O*) so labelled because it coincides with the isolator elastic center in this case. The transformation matrix is defined,

$$[T(R_y, R_z)]_O = \begin{bmatrix} 1 & 0 & 0 \\ 0 & 1 & 0 \\ -R_{z,O} & R_{y,O} & 1 \end{bmatrix}, \tag{2}$$

which allows conversion of forces and displacements from a coordinate system at *O* to one at *G*,

$$\{F\}_G = [T]_O \{F\}_O, \tag{3}$$

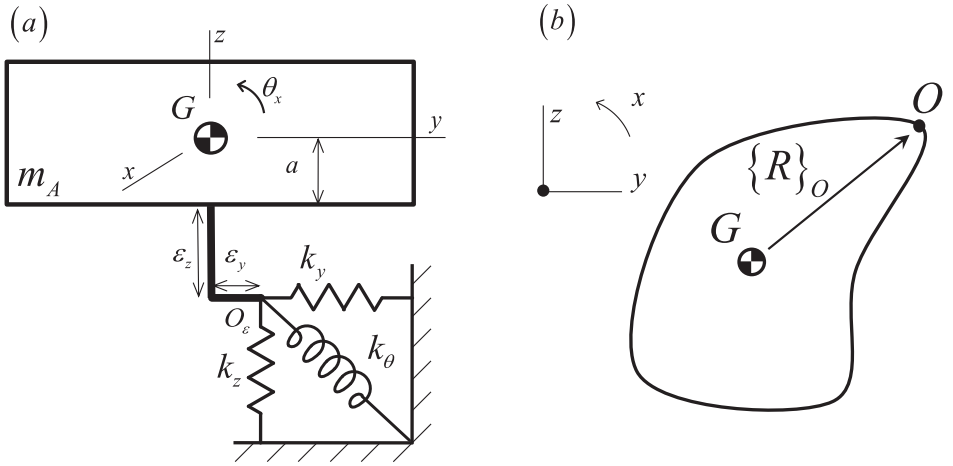

Fig. 5. (*a*) Analytical 3-DOF model for the isolation system configuration *T-A* of Fig. 2(a). Here, k_y, k_z, and k_θ are the diagonal stiffness elements acting at the elastic center *O*, m_A is the mass supported by the isolator, ε_z and ε_y are the vertical and lateral distances from the hard point to the elastic center, respectively, and *a* is the distance from *G* to the hard point; (*b*) Generalized rigid body system, where $\{R\}_O = \{R_{y,O}, R_{z,O}\}$ is a vector from the center of gravity *G* to an attachment point *O*, which at this point is the isolator's elastic center. Forces and displacements applied to the body at *O* may be transformed to effective quantities at *G* using the transformation matrix $[T(R_y, R_z)]_O$.

$$\{q\}_O = [T]_O^T \{q\}_G. \tag{4}$$

Applying this equation to the example system by using Eqs. (3) and (4) with (1) for the static case ($\omega = 0$) leads to $\{F\}_G = [T]_O[K]_O[T]_O^T\{q\}_G$. Thus,

$$[K]_G = [T]_O[K_O][T]_O^T = \begin{bmatrix} k_y & 0 & k_y(a+\varepsilon_z) \\ 0 & k_z & \varepsilon_y k_z \\ k_y(a+\varepsilon_z) & \varepsilon_y k_z & k_z\varepsilon_y^2 + k_y(a+\varepsilon_z)^2 + k_\theta \end{bmatrix}. \tag{5}$$

The elastic coupling between the y and θ_x directions is proportional to $(a+\varepsilon_z)$, while the z – θ_x coupling is proportional to ε_y. No coupling is present between the shear and bounce directions, and since $\varepsilon_y = 0$ for the axisymmetric isolator being examined, the z (bounce) direction becomes entirely uncoupled. The system's rotational stiffness at G is affected by all three spring constants, though the effect of k_θ may be overshadowed by the other two terms, depending on the geometry. Thus the physical systems designed for identification purposes should seek to limit ε_y and ε_z (where possible) to ensure that k_θ plays a distinct role and may be determined. Prior literature [15] has ignored the k_θ term, assuming it to have negligible effect compared to the k_y and k_z terms, whereas the proposed method allows for a quantitative evaluation of this hypothesis. Later it will be seen that the k_θ term is quite large for some of the example cases.

3.4. Eigensolution and extraction of stiffness terms

Natural frequencies (ω_n) for the 3-DOF undamped system are related to the stiffness matrix in terms of the characteristic equation,

$$\left|[K]_G - \omega_n^2[M]\right| = 0, \tag{6}$$

and the eigenvectors $\{\phi_n\}$ are given in terms of the eigenvalue problem,

$$\left([K]_G - \omega_n^2[M]\right)\{\phi_n\} = \{0\}. \tag{7}$$

Typically, eigenvectors are normalized such that $[\phi]^T[K]_G[\phi] = [\Lambda]$ and $[\phi]^T[M][\phi] = [I]$, where $[\Lambda] = diag\left[\omega_n^2\right]$ and $[\phi] = [\cdots\{\phi_n\}\cdots]$, though alternative normalization schemes may be used. If $\{\phi_n\}$ are precisely known, then a unique solution for k_y, k_z, and k_θ may be obtained from Eq. (7). First, since (7) is valid for each modal index n, they may be combined into matrix form to yield the following,

$$[K]_G[\phi] = [M][\phi][\Lambda]. \tag{8}$$

Using Eqs. (5) and (8) yields an explicit, unique solution for the fundamental stiffness values as,

$$[K]_O = [T]_O^{-1}[M][\phi][\Lambda][\phi]^{-1}\left([T]_O^T\right)^{-1}. \tag{9}$$

However, this calculation is relatively sensitive to error in an estimated modal matrix since accurate eigenvectors are necessary to directly use equation (9). Further, since only one accelerometer is used in the modal experiments, measured rotations ($\theta_x(t)$ in this case) are not available and so neither are experimental modeshapes. The above mentioned shortcoming may be addressed in one of three ways. First, enhancing the experimental procedure to include additional sensors to capture all relevant displacements and rotations would allow for the direct estimation of eigenvectors but could increase the chances of experimental complications; however, this is left for future work. Second, eigenvectors may be estimated from the finite element model $\left(\left[\hat{\phi}\right]\right)$ and substituted into Eq. (9) to estimate $[K]_O$ as $diag\left[\hat{k}_y, \hat{k}_z, \hat{k}_\theta\right]$, where the hat symbol indicates an estimated value. This solution is perhaps the simplest, but it does rely upon accurate finite element models of the elastomeric mount. The third approach is to use the Eq. (6) instead of (7) as the basis for stifness estimation. The equation is reduced to dimension 2 by removing the z direction (assuming $\varepsilon_y = 0$, as before) to reduce the algebraic complexity, and then solving the characteristic polynomial for $\hat{k}_y$ and $\hat{k}_\theta$,

$$\begin{vmatrix} \hat{k}_y - \omega_n^2 m_A & \hat{k}_y(a+\varepsilon_z) \\ \hat{k}_y(a+\varepsilon_z) & \hat{k}_y(a+\varepsilon_z)^2 + \hat{k}_\theta - \omega_n^2 J_{xxA} \end{vmatrix} = 0; \quad n = 1, 3. \tag{10}$$

This leads to eight possible solution sets for $\hat{k}_y$ and $\hat{k}_\theta$, but for all example cases in this study, only one is physically realizable with both $\hat{k}_y, \hat{k}_\theta > 0$. The third stiffness term is easily calculated from the uncoupled mode,

$$\hat{k}_z - \omega_n^2 m_A = 0; \quad n = 2 \tag{11}$$

This third solution is tractable for a simple system such as configuration *T-A*, especially where the equations can be decoupled to a maximum of 2-DOF. For a more complicated system, however, the estimation could become unwieldy. It is also possible that some parameter sets may yield non-unique, physically realizable solutions.

4. Discussion of stiffness results

4.1. Application of proposed identification procedure

The two stiffness extraction solution methods (as discussed in the previous section) converge to the same $\hat{k}$ values, which are given in Table 2 for each laboratory isolator. Although the relative value of $\hat{k}_\theta$ compared to $\hat{k}_y$ or $\hat{k}_z$ is difficult to directly evaluate since the units are different, comparison of the terms of the (3,3) element of $[K]_G$ in Eq. (5) allows for comparison in the same units. Here, it is found that $\hat{k}_\theta$ is between about 3 and 8 times $k_y(a+\varepsilon_z)^2$ for each isolator, suggesting that the $\hat{k}_\theta$ term is not generally negligible; this contradicts the usual assumption made in prior work [15]. Further, roughly a 50% increase is observed in the vertical/lateral stiffness ratio, which influenced dynamic scaling when it comes to damping—this will be discussed further in the next section.

The stiffness solutions can be verified by calculating the analytical eigenvectors by solving Eqs. (7) using (5) and the values of $\hat{k}_y$, $\hat{k}_z$, and $\hat{k}_\theta$. (For this example case, each method converges to the same solution.) These analytical eigenvectors ($\{\phi\}$) are compared with the finite element eigenvectors $\left\{\hat{\phi}_n\right\}$ using the modal assurance criterion (MAC) [17],

$$MAC(n) = \frac{\left|\{\phi_n\}^T\left\{\hat{\phi}_n\right\}\right|^2}{\left(\{\phi_n\}^T\{\phi_n\}\right)\left(\left\{\hat{\phi}_n\right\}^T\left\{\hat{\phi}_n\right\}\right)}. \tag{12}$$

The resulting modal matrices for Isolator I (in SI units) are normalized again for clarity and compared,

$$[\phi] = \begin{bmatrix} 1 & 0 & 0 \\ 0 & 0 & 1 \\ -8.5 & 1 & 0 \end{bmatrix}, \quad \left[\hat{\phi}\right] = \begin{bmatrix} 1 & 0 & 0 \\ 0 & 0 & 1 \\ -15.2 & 1 & 0 \end{bmatrix}, \tag{13a, b}$$

with MAC values in excess of 99% for all three modes, indicating an accurate estimation of the stiffness matrix for Isolator I. The same process is repeated for all of the other isolators in this study, and similar results are obtained.

4.2. Determination of Young's modulus (E)

The E value associated with each isolator may be estimated using finite element models of each modal test configuration (*T-A*, *T-B* or *T-C*). The $\hat{E}$ parameter in the model is tuned by comparing finite element estimations of natural frequencies $\{\hat{\omega}_n\}$ with measured natural frequencies $\{\omega_n\}$, recognizing that $\omega_n \propto \sqrt{E}$; if $\{\hat{\omega}_n\} \approx \{\omega_n\}$, then $\hat{E} \approx E$. These $\hat{E}$ are compiled in Fig. 6 for different system configurations and isolators, showing an overall trend between E and S, where E_r is a reference value used for normalization. Similarly, the stiffness values of Isolator V roughly follow the relation, $\hat{k}_y, \hat{k}_z, \hat{k}_\theta \propto \hat{E}$, although not perfectly. This may be due to the composite effect of the metal insert as shown in Fig. 1.

It is seen that somewhat higher estimated variation (around 6.3%) exists at 68 S than for lower S values. There may be several contributing factors causing this variation in E. First, the higher slope of the E vs. S curve at the higher hardness values indicates increased sensitivity to S, so even a small change in the material properties may produce significant variation in E. Second, different values of S and different system masses both lead to different system natural frequencies. The true dynamic stiffness of any rubber material is likely frequency dependent, so $\hat{k} \approx k(\omega_n)$. If the dynamic stiffness spectrum is not relatively uniform in the frequency range of interest, different $\hat{k}$ and subsequently $\hat{E}$ values may be obtained. Finally, the different system masses in the various configurations may be introducing a preload effect, but since the operating point was chosen in a relatively linear regime, this should not cause significant variation in $\hat{E}$ estimation.

A curve fit is applied to the data points in Fig. 6 using the following rational function, where γ and λ are the coefficients used in the numerator and denominator:

$$\hat{E}(S_A) = \frac{\sum_{i=0}^{3}\gamma_i S^i}{\sum_{i=0}^{3}\lambda_i S^i}. \tag{14}$$

Table 2
Estimated diagonal stiffness elements ($\hat{k}_y$, $\hat{k}_z$, and $\hat{k}_\theta$) and $\hat{k}_z/\hat{k}_y$ ratios for four laboratory isolators.

Isolator Designation	Material	S	k_y (N/mm)	k_z (N/mm)	k_θ (kN·mm/rad)	k_z/k_y
I	Polyurethane	40	12	115	40	9.6
II	Polyurethane	60	28	224	72	8
III	Silicone	60	18	267	94	14.8
IV	EPDM	60	101	1453	630	14.4

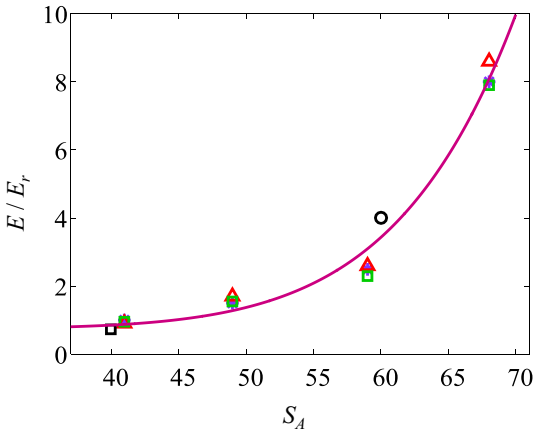

Fig. 6. Comparison of computed Young's modulus (E) as a function of Shore A durometer (S) across all three configurations using both laboratory and production isolators. Key: ✱ – Configuration *T-A* with isolator V; △ – Configuration *T-B* with isolator V; □ – Configuration *T-C* with isolator V; ■ – Configuration *T-A* with isolator I; ○ – Configuration *T-A* with isolator IV; ▬ – Curve fit using all data points. Here, E_r is a reference value used for the normalization.

Eq. (14) is proposed here since it is sufficiently general to capture both the new data from this study and approximate historical relationships between E and S [16,18]. The values of γ and λ obtained for the new data shown in Fig. 6 are $\{\gamma_0, \gamma_1, \gamma_2, \gamma_3, \lambda_0, \lambda_1, \lambda_2, \lambda_3\}$ = {489.9, 8642, −1857, 41.43, 1579, 11330, −210.5, 1}; for the relationship reported in [16] they are {290.7, 6090, 801.8, −4.30, 220.2, 19360, −293.6, 1}; and for the relationship in [18]: {−167.5, −3490, 403.6, −3.63, 621.3, 11380, −213.8, 1}. The trend of the curve in Fig. 6 is qualitatively similar to that reported in the literature [16,18] but quantitatively, the expressions obtained from the literature deviate substantially from our results. This suggests that the E vs. S relationship may be more tenuous than previously suggested [16,18], especially where complex geometry may exacerbate non-uniform material properties due to molding, curing, etc. Further attention to this issue is needed in future work.

5. Identification of dissipation properties

5.1. Structural damping formulation

The real-valued eigensolution basis that is employed for stiffness identification inherently ignores the internal damping of the isolator(s). Therefore, measured $\tilde{A}(\omega)$ spectra from configuration *T-A*, as illustrated in Fig. 7, are utilized to assess material damping (only within the isolators) in terms of several well-known formulations. Frequency invariant structural damping is one common model which applies a single, global value in the following form, where η is the mode-independent loss factor, and tilde implies a complex-valued quantity in the frequency domain,

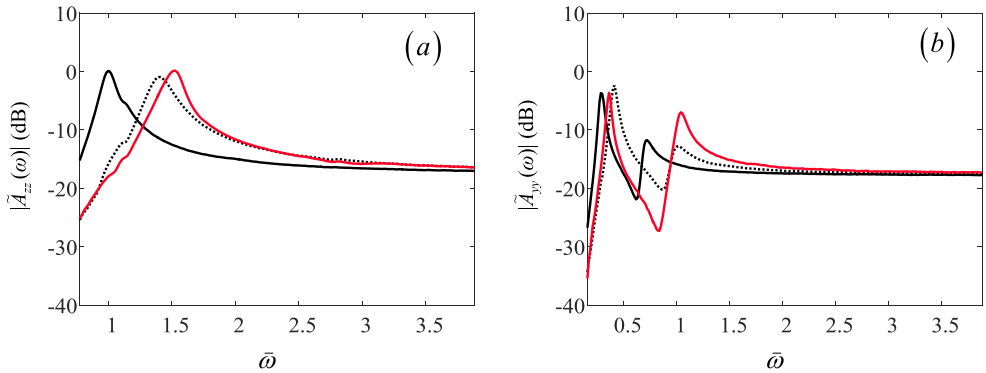

Fig. 7. Measured $\left|\tilde{A}(\omega)\right|$ magnitude spectra for three annular laboratory isolators under configuration *T-A*, including (*a*) $\left|\tilde{A}_{zz}(\omega)\right|$ and (*b*) $\left|\tilde{A}_{yy}(\omega)\right|$, where $\bar{\omega}$ is the normalized frequency. Key: ▬ – Isolator I; ····· – Isolator II; ▬ – Isolator III.

$$\left[\tilde{K}\right]_O = [K]_O(1 + \mathrm{i}\eta). \tag{15}$$

The half-power bandwidth method [19] is employed to estimate the value of η from $\tilde{A}_{zz}(\omega) = -\omega^2 u_z/F_z|_\omega$ and $\tilde{A}_{yy}(\omega) = -\omega^2 u_y/F_y|_\omega$ spectra obtained from modal experiments for all laboratory isolators in test configuration *T-A*. Measured values of η (determined from the uncoupled mode in the $\tilde{A}_{zz}(\omega)$ spectra) for the isolators used in this study range from 11% to 19% with an arithmetic mean of 12.5%. This is close to values reported in the literature [20]. Coupled rocking type modes are not used to estimate η since the $\tilde{A}_{yy}(\omega)$ spectrum has two closely spaced resonant peaks and the half-power method assumes a single, distinct peak. Further, an anti-resonance is very close to the coupled rocking mode in $\tilde{A}_{yy}(\omega)$, distorting the frequency response curve and thereby slanting the η estimation. Accordingly, the mean η adopted from $\tilde{A}_{zz}(\omega)$ is used as the global value. The damped analytical model is then characterized in terms of the accelerance matrix,

$$\left[\tilde{A}(\omega)\right] = \begin{bmatrix} \tilde{A}_{yy}(\omega) & 0 & \tilde{A}_{y\theta}(\omega) \\ 0 & \tilde{A}_{zz}(\omega) & 0 \\ \tilde{A}_{\theta y}(\omega) & 0 & \tilde{A}_{\theta\theta}(\omega) \end{bmatrix} = -\omega^2\left(-\omega^2[M] + [K]_G(1 + \mathrm{i}\eta)\right)^{-1}, \tag{16}$$

and the resulting $\tilde{A}_{yy}(\omega)$ and $\tilde{A}_{zz}(\omega)$ spectra may be directly compared with the measured accelerance spectra as shown in Fig. 8. Good agreement is achieved between estimated and measured $\left|\tilde{A}_{zz}(\omega)\right|$ spectra for three laboratory isolators, but the estimated $\left|\tilde{A}_{yy}(\omega)\right|$ spectra agree with measurements primarily only in terms of the resonant peak frequencies and not the peak amplitude, particularly for the second mode. To address this discrepancy, mode-dependent damping is considered using a viscous damping formulation.

5.2. Identification of viscous damping matrix

Since the *T-A* system has distinct physical stiffness and mass elements, proportional damping is assumed with the Rayleigh damping approximation. This model expresses the damping matrix $[C]_G$ as a linear combination of the mass and stiffness matrices: $[C]_G = \beta_M[M] + \beta_K[K]_G$ where β_M and β_K are the proportionality constants. Since the mass element is rigid and made of virtually undamped metal, β_M is assumed to be zero. Thus β_K is estimated at a given mode n, and indeed there are

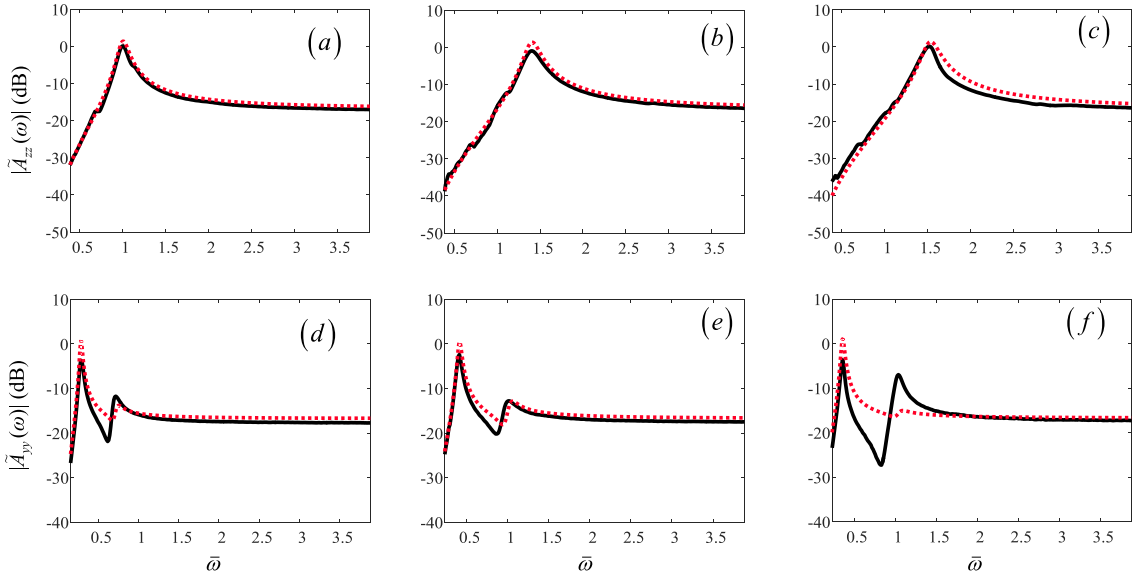

Fig. 8. Comparison of estimated and measured $\left|\tilde{A}(\omega)\right|$ magnitude spectra for three annular laboratory isolators under configuration *T-A* given global, mode-independent loss factor, η= 12.5%: (*a*) $\left|\tilde{A}_{zz}(\omega)\right|$ for Isolator I, (*b*) $\left|\tilde{A}_{zz}(\omega)\right|$ for Isolator II, (*c*) $\left|\tilde{A}_{zz}(\omega)\right|$ for Isolator III, (*d*) $\left|\tilde{A}_{yy}(\omega)\right|$ for Isolator I, (*e*) $\left|\tilde{A}_{yy}(\omega)\right|$ for Isolator II, (*f*) $\left|\tilde{A}_{yy}(\omega)\right|$ for Isolator III. Key: ▬ – Measurement; ▪▪▪ – Analytical model.

three possible values for β_K that can be obtained from the modal domain relation given by $\zeta_n = \beta_K \omega_n/2$, where ζ_n are the modal damping ratios. Now, damping estimates include the coupled modes in the $\tilde{A}_{yy}(\omega)$ spectrum as well. The three solutions of the Rayleigh formulation yield inconsistent values of $[C]_G$ elements with no suggestion of which to choose, and thus its utility is severely limited.

More generally, the viscous damping matrix $[C]_G$ may be constructed using the orthogonality of modes, where $\left[\bar{\phi}\right]$ is the normalized modal matrix and ζ_n are the measured damping ratios:

$$[C]_G = \begin{bmatrix} C_{yy} & C_{yz} & C_{y\theta} \\ C_{zy} & C_{zz} & C_{z\theta} \\ C_{\theta y} & C_{\theta z} & C_{\theta\theta} \end{bmatrix} = \left(\left[\bar{\phi}\right]^T \right)^{-1} diag[2\omega_n \zeta_n] \left[\bar{\phi}\right]^{-1}. \tag{17}$$

The $[C]_G$ calculated by this method may require conditioning since arbitrary modal damping values may introduce physically unrealizable damping terms. For the case of configuration *T*-A, any $C_{z\theta}, C_{\theta z} \neq 0$ or $C_{yy}, C_{zz}, C_{\theta\theta} < 0$ terms are set to zero. After the conditioning process, the resulting modal damping ratios $\hat{\zeta}_n$ are calculated from the conditioned damping matrix $\left[\hat{C}\right]_G$,

$$diag\left[\hat{\zeta}_n\right] = diag\left[\frac{1}{2\omega_n}\right] \left[\bar{\phi}\right]^T \left[\hat{C}\right]_G \left[\bar{\phi}\right], \tag{18}$$

and it may be determined whether the conditioning has introduced unacceptable discrepancy between $\hat{\zeta}_n$ and ζ_n. However, for laboratory isolators I, II, and III, conditioning of $[C]_G$ has not been found to be necessary.

For the sake of illustration, the calculated viscous damping matrix for isolator I is found to be as follows with pertinent units,

$$[C_I]_G = \begin{bmatrix} 0.0176\ \text{N}\cdot\text{s/mm} & 0 & -0.260\ \text{N}\cdot\text{s/rad} \\ 0 & 0.0340\ \text{N}\cdot\text{s/mm} & 0 \\ -0.260\ \text{N}\cdot\text{s} & 0 & 39.9\ \text{N}\cdot\text{mm/rad} \end{bmatrix}. \tag{19}$$

The damping matrices for isolators II and III are normalized element-wise by $[C_{G,I}]$ as expressed above for the sake of comparison,

$$\left[\bar{C}_{II}\right]_G = \begin{bmatrix} 1.2 & 0 & 0.5 \\ 0 & 1.9 & 0 \\ 0.5 & 0 & 0.7 \end{bmatrix}, \quad \left[\bar{C}_{III}\right]_G = \begin{bmatrix} 0.7 & 0 & 0.4 \\ 0 & 1.5 & 0 \\ 0.4 & 0 & 0.7 \end{bmatrix}. \tag{20-a, b}$$

Interestingly, all three isolators have relatively similar damping matrices despite differences in material, durometer, and geometry; however, a qualitative difference exists between these $[C]_G$ matrices and $[K]_G$, since the off-diagonal damping elements are negative. This suggests an alternate coupling mechanism other than the kinematic coupling which produces the off-diagonal stiffness elements. Further, it was previously seen in Eq. (5) that transforming the coordinate system to *O* would diagonalize $[K]_G$, but it is now observed that this is not the case for $[C]_G$,

$$[C_I]_O = \begin{bmatrix} 0.0176\ \text{N}\cdot\text{s/mm} & 0 & -0.779\ \text{N}\cdot\text{s/rad} \\ 0 & 0.0340\ \text{N}\cdot\text{s/mm} & 0 \\ -0.779\ \text{N}\cdot\text{s} & 0 & 69.9\ \text{N}\cdot\text{s}\cdot\text{mm/rad} \end{bmatrix}. \tag{21}$$

This suggests that there may exist a "dissipative center" which is distinct from the elastic center and has no physical coupling from the damping perspective. The physical significance of this should be investigated in further studies.

The system response under the viscous damping formulation is defined in terms of the accelerance matrix,

$$\left[\tilde{A}(\omega)\right] = -\omega^2 \left(-\omega^2 [M] + i\omega [C]_G + [K]_G\right)^{-1}. \tag{22}$$

Viscously damped $\left|\tilde{A}_{yy}(\omega)\right|$ spectra are compared with measurement in Fig. 9. Discussion of the $\left|\tilde{A}_{zz}(\omega)\right|$ comparisons is ignored here for brevity, since the analysis for the uncoupled mode is trivial, and good accuracy is achieved without difficulty. In the *y* direction, however, the expected boost in accuracy from the inclusion of a mode-dependent damping formulation is not achieved. In particular, the second mode shows less agreement with mode-dependent viscous damping than with global structural damping due, in part, to distorted estimation of ζ_n from the coupled modes in $\tilde{A}_{yy}(\omega)$. Some insight into this discrepancy is available through a more rigorous modal analysis in the next section.

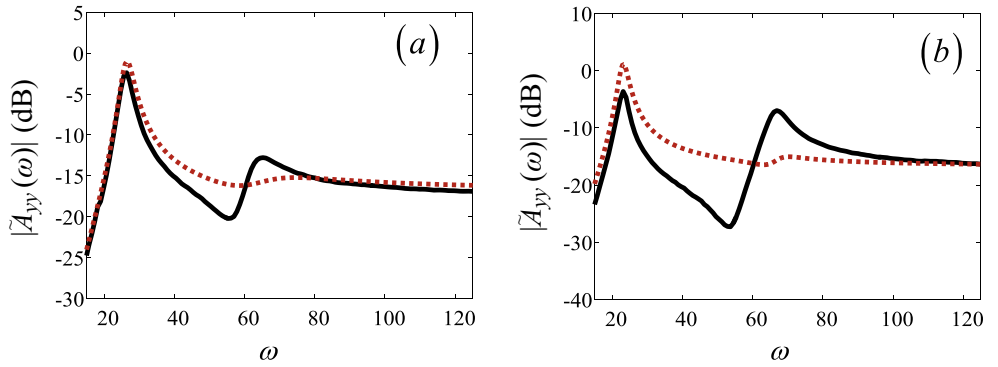

Fig. 9. Measured $\left|\tilde{A}_{yy}(\omega)\right|$ spectra for (*a*) Isolator II and (*b*) Isolator III isolators under configuration *T-A* compared with analytical estimates using the viscous damping formulation. Isolator I behaves similar to II so these spectra are not shown. Key: ▬ – Measurement; ▪▪▪ – Analytical model.

5.3. Examination of damping model using modal decomposition

In Fig. 9, the analytical model's response ostensibly shows excessive damping in the second coupled mode when compared with the measurement. However, the underlying cause stems primarily not from the damping model, but from a relatively lower contribution of the second mode that is essentially masked by the first mode. This explanation is verified by inspecting the response of the system in the modal domain, and then comparing model with measurement. Since rotational motion was not measured in the proposed identification method, $\theta_x(\omega)$ is estimated from the measured $u_y(\omega)$ by assuming modal decomposition where $\xi_n(\omega)$ is the response of the nth mode, and h_n is an amplitude coefficient which corrects for arbitrary normalization of $[\phi]$,

$$\begin{Bmatrix} u_y(\omega) \\ \theta_x(\omega) \end{Bmatrix} = \begin{Bmatrix} \phi_{1,1}\xi_1(\omega) + \phi_{2,1}\xi_2(\omega) \\ \phi_{1,2}\xi_1(\omega) + \phi_{2,1}\xi_2(\omega) \end{Bmatrix}, \tag{23}$$

$$\xi_n(\omega) = \frac{h_n}{\omega_n^2 - \omega^2 + \mathrm{i}2\omega\omega_n\zeta_n} \tag{24}$$

Eigenvectors are taken from the finite element model, a curve fit is applied to identify the optimal h_n, ω_n, and ζ_n for both modes, and these are used to estimate $\theta_x(\omega)$ from Eq. (23). The modal decomposition of $u_y(\omega)$ is shown in terms of accelerance in Fig. 10. If additional sensors may be deployed to measure the rotation directly during the experimental procedure described in Section 3.2, the preceding steps could be skipped. It is readily apparent from Fig. 10 that estimations for the damping of the first mode will not be affected by using the modal decomposition; however, both the apparent natural frequency and damping ratio are changed for the second mode. Enhanced accuracy for both stiffness and damping identification is obtained through modal decomposition, so it is employed in both ω_n and ζ_n estimation throughout this study.

The modal domain response is then calculated from the familiar equation,

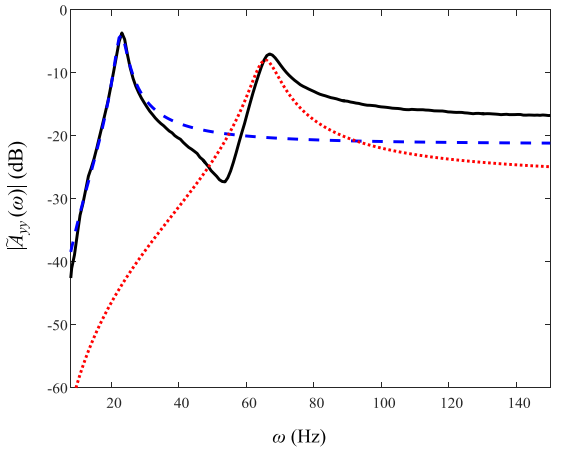

Fig. 10. The modal decomposition of $u_y(\omega)$ for isolator III in terms of $\left|\tilde{A}_{yy}(\omega)\right|$. Key: ▬ – Measurement; ▬ ▬ – Shear mode; ▪▪▪ – Rocking mode.

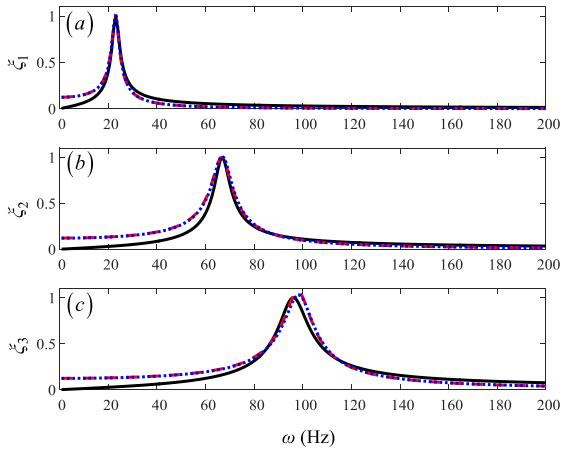

Fig. 11. Comparison of estimated and measured $\xi(\omega)$ magnitude spectra for isolator III under configuration *T-A*. Modal decomposition is carried out to evaluate damping characterization. The measured response of all three modes is normalized and compared with the analytical model in the modal domain, using the structural and viscous damping. Key: ——— – Measurement; – – – – Analytical model ([C]); ····· – Analytical model ([η]).

$$\{\xi\} = [\phi]^{-1}\{q\}, \tag{25}$$

and each mode may then be treated separately. The measured response of all three modes is normalized and compared with the analytical model in the modal domain in Fig. 11 for isolator III, using both structural and viscous damping formulations, showing that either damping formulation adequately captures the measured dissipative property for this device. Estimated modal damping ratios are given for isolators I, II, and III in Table 3 and used to estimate $[C]_G$ in the analytical model using Eq. (17) for each case. The $\left|\tilde{A}_{yy}(\omega)\right|$ spectra is calculated for Isolator II using both structural and viscous damping formulations and compared with measurements in the physical domain in Fig. 12. Overall, reasonable damping estimation is achieved, as well as resolution of the difficulties associated with direct estimation of modal damping ratios.

While both damping formulations used in this article offer a reasonable estimation of the isolators' dissipative properties, some predictions show a small shift in resonant and anti-resonant frequencies when compared to measurements. This is especially true for the anti-resonances depicted in Fig. 8 and may be due to frequency dependent characteristics, $[C(\omega)]_G$, which are not captured by the Kelvin-Voigt model used here. Alternative viscoelastic models such as the Maxwell, Standard or other models [21] may better capture frequency dependence of the dissipative elements, but this effort is left for future investigations.

6. Experimental validation of identification process

6.1. Identification process for laboratory isolators under configuration T-B

Fig. 13 depicts the analytical system model for the configuration *T-B* (of Fig. 2(b)) that supports a horizontal thick plate on 4 identical isolators. This setup is used to validate the proposed identification process based on configuration *T-A* to obtain $[K]_O$ (of dimension 3), first for the laboratory isolators. The isolator properties, namely $[K]_O$ and the location of *O* (with eccentrics ε_y and ε_z) identified as previously using configuration *T-A*, are used in the analytical model for each isolator of configuration *T-B*. Each stiffness block (with 3 diagonal elements and a kinematic link) is used to represent two identical isolators in Fig. 13. The analytical model again captures the in-plane dynamics of *T-B* in the *y-z* plane assuming physical symmetry; this representation may be used for the *x-z* plane as well though this is not described here.

The governing equations for the undamped isolation system (from the static equilibrium under a given preload) for Fig. 13 follow the same form as Eq. (1), where the generalized displacement $\{\mathrm{q}(t)\} = [u_y(t)\ u_z(t)\ \theta_x(t)]^{\mathrm{T}}$ is used as before

Table 3
Estimated modal damping ratios (ζ_n) of configuration *T-A* using modal decomposition in shear ($n = 1$), rocking ($n = 2$) and bounce ($n = 3$) modes.

Isolator Designation	Material	*S*	ζ_1 (%)	ζ_2 (%)	ζ_3 (%)
I	Polyurethane	40	8.0	5.9	6.7
II	Polyurethane	60	7.3	7.1	7.5
III	Silicone	60	6.7	5.8	6.1

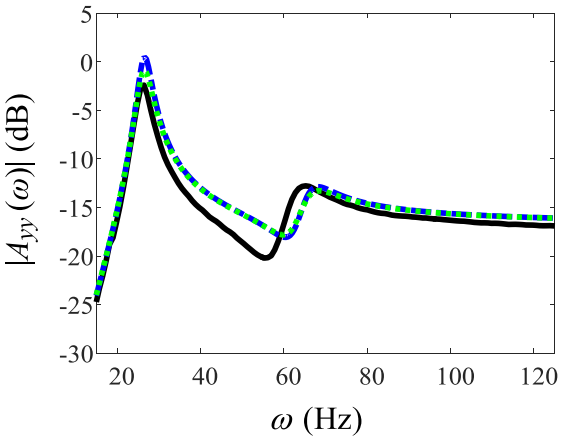

Fig. 12. Comparison of estimated and measured $\left|\tilde{A}_{yy}(\omega)\right|$ spectra for isolator II under excitation of configuration *T-A* in the *y* direction. Key: ▬ – Experiment; Analytical model (mode-independent η); ┈┈ – Analytical model ($[C]_G$ from modal decomposition).

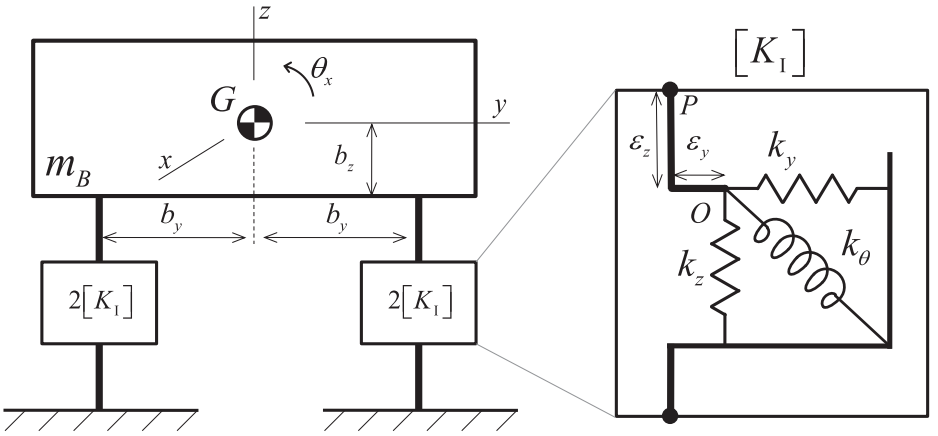

Fig. 13. Analytical 3-DOF model for the 4-mount isolation system under configuration *T-B* of Fig. 2(b). The block on the right indicates the sub-system model which is contained within a single $[K_I]$ element (for isolator I as shown), k_y, k_z, and k_θ are the diagonal stiffness elements acting at the isolator's elastic center. Here, ε_z and ε_y are the vertical and lateral elastic center coordinates, m_B is the rigid mass, and b_y, b_z locate the isolator hard points from the center of gravity.

for a coordinate system centered at *G*, {*F*} is the dynamic (external) force vector acting at *G*. The mass matrix is given by $[M] = diag[m_B, m_B, J_{xxB}]$, and the system stiffness matrix $[K]_G$ (about *G*) is defined as,

$$[K]_G = 2\left[T\left(-b_y+\varepsilon_{y,\boldsymbol{I}},-b_z-\varepsilon_{z,\boldsymbol{I}}\right)\right][K_{\boldsymbol{I}}]\left[T\left(-b_y+\varepsilon_{y,\boldsymbol{I}},-b_z-\varepsilon_{z,\boldsymbol{I}}\right)\right]^T + 2\left[T\left(b_y+\varepsilon_{y,\boldsymbol{I}},-b_z-\varepsilon_{z,\boldsymbol{I}}\right)\right][K_{\boldsymbol{I}}]\left[T\left(b_y+\varepsilon_{y,\boldsymbol{I}},-b_z-\varepsilon_{z,\boldsymbol{I}}\right)\right]^T$$
$$= \begin{bmatrix} 4k_y & 0 & 4k_y(b_z+\varepsilon_z) \\ 0 & 4k_z & 4\varepsilon_y k_z \\ 4k_y(b_z+\varepsilon_z) & 4\varepsilon_y k_z & 4k_z(b_y^2+\varepsilon_y^2)+4k_y(b_z+\varepsilon_z)^2+4k_\theta \end{bmatrix}. \quad (26)$$

An interaction between isolators is observed which, in some ways, mimics configuration *T-A*. The lateral placement of isolators (b_y) does not affect any coupling terms since the generated moments cancel each other as long as symmetry exists about *G*. The rotational stiffness element, however, is affected.

The eigenvalue problem for the above model is solved and the estimated values of ω_n (in Hz) for isolator I from the 3-DOF analytical system model are $\omega_n = 10,\ 31,$ and 35 Hz. The corresponding measured values of ω_n obtained using the experimental system are found to be 12, 28, and 34 Hz, suggesting reasonable prediction accuracy, and validation for the stiffness terms as given previously in Table 3. Some prediction error may be observed between analytical and experimental ω_n values from configuration *T-B* for isolators I, II, and III, and these are compared in Table 4. Overall, the errors are small, but the first two modes with isolator III show a substantial error. This is likely due to a more nonlinear static force–deflection curve such that the additional preload under configuration *T-B* has shifted the operating point, introducing error to $[\hat{K}]_O$. Accelerance

Table 4
Measured and predicted natural frequencies (ω_n) for shear ($n = 1$), bounce ($n = 2$) and rocking ($n = 3$) modes under configuration *T-B* natural with laboratory isolators.

Isolator Designation	Material	S	Measured (Hz)			Predicted (Hz)		
			ω_1	ω_2	ω_3	ω_1	ω_2	ω_3
I	Polyurethane	40	12	28	34	10	31	35
II	Polyurethane	60	17	40	47	15	43	48
III	Silicone	60	19	43	50	12	47	52

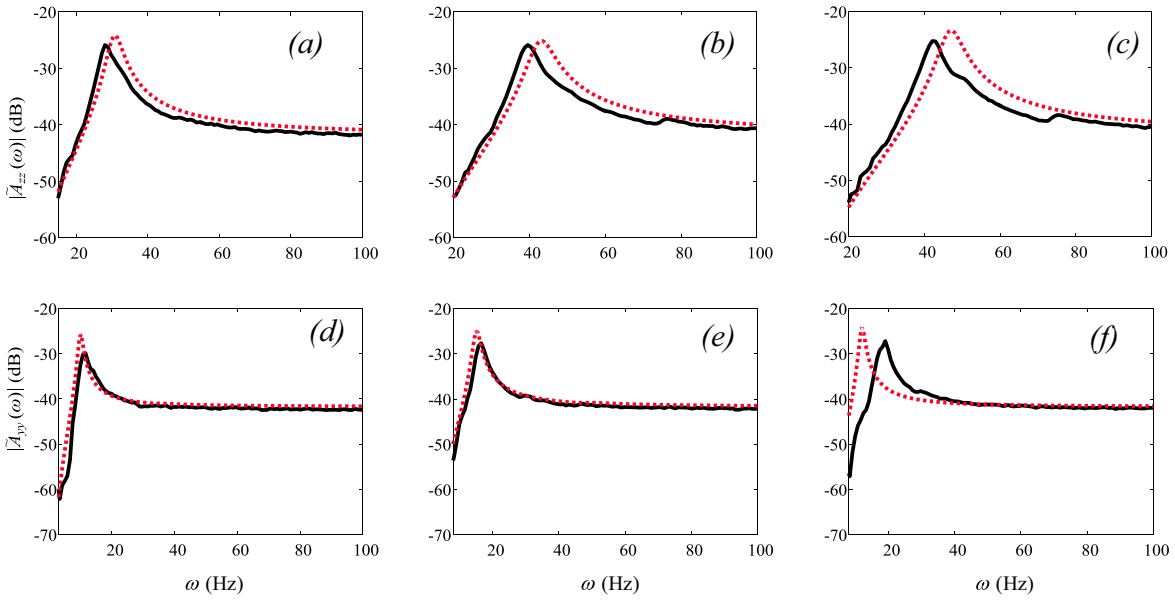

Fig. 14. Comparison of measured and predicted $\left|\tilde{A}(\omega)\right|$ spectra for three annular laboratory isolators under configuration *T-B*. (*a*) $\left|\tilde{A}_{zz}(\omega)\right|$ for Isolator I, (*b*) $\left|\tilde{A}_{zz}(\omega)\right|$ for Isolator II, (*c*) $\left|\tilde{A}_{zz}(\omega)\right|$ for Isolator III. (*d*) $\left|\tilde{A}_{yy}(\omega)\right|$ for Isolator I, (*e*) $\left|\tilde{A}_{yy}(\omega)\right|$ for Isolator II, (*f*) $\left|\tilde{A}_{yy}(\omega)\right|$ for Isolator III. Key: ▬ – Measurement; ▪▪▪ – Analytical model.

magnitude spectra $\left|\tilde{A}_{zz}(\omega)\right|$ and $\left|\tilde{A}_{yy}(\omega)\right|$ are obtained for configuration *T-B* using the component-level viscous damping formulation of Eq. (17) from configuration *T-A*. These are compared with measurements in Fig. 14 for isolators I, II, and III. For the $\left|\tilde{A}_{zz}(\omega)\right|$ spectra, the analytical model slightly over-predicts the natural frequency. This is likely due to the assumption of plate rigidity—a flexible plate softens the system, decreasing the natural frequency. Only one strong resonant peak is visible in the $\left|\tilde{A}_{yy}(\omega)\right|$ spectra for all example cases, whereas two are present for configuration *T-A* as discussed previously in Section 5. This is because the distribution of elastic properties to four isolators allows them to work in tandem, stabilizing the system and reducing the inherent coupling between shear and rocking motions. In fact, more coupling would be induced between the z and θ_x directions if a force, F_z, were to be applied offset from the CG; indeed, very small peaks are visible in the $\left|\tilde{A}_{zz}(\omega)\right|$ spectra. Finally, good agreement is achieved in the $\left|\tilde{A}_{yy}(\omega)\right|$ spectra for both polyurethane isolators, but the model substantially under-predicts the natural frequency for the silicone mount. This is likely attributable to the significant nonlinearity of many silicone rubbers which may be in play even at small amplitudes [22].

6.2. Identification of production isolators under configuration T-B

Similar steps are carried out using a production isolator (V) shown in Fig. 1(b) which is tested for four S values (41, 49, 59 and 68). Fig. 15 shows the comparison of the measured and estimated $\left|\tilde{A}(\omega)\right|$ spectra for isolator V under configuration *T-A*, indicating good characterization of the device. Fig. 16 shows the comparison of measured and predicted $\left|\tilde{A}(\omega)\right|$ magnitude

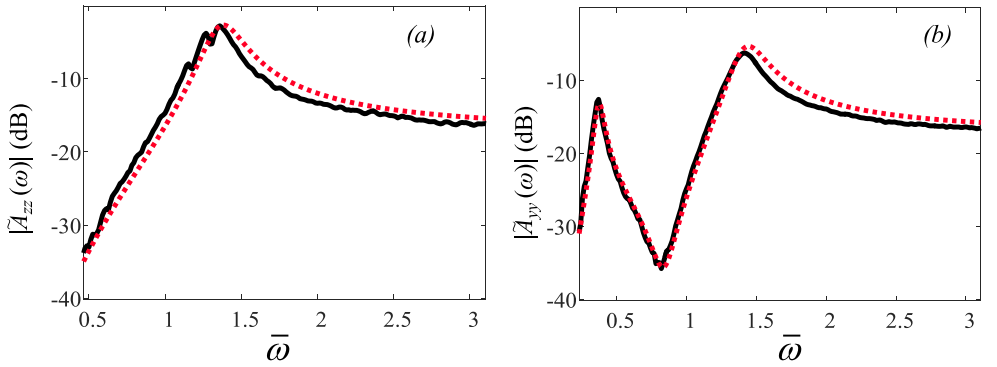

Fig. 15. Comparison of estimated and measured $\left|\tilde{A}(\omega)\right|$ spectra for the production isolator (V) under configuration *T-A*, in particular: (*a*) $\left|\tilde{A}_{zz}(\omega)\right|$ (*b*) $\left|\tilde{A}_{yy}(\omega)\right|$, where $\bar{\omega}$ is the normalized frequency. Key; ▬ – Measurement; ▪▪▪ – Analytical model.

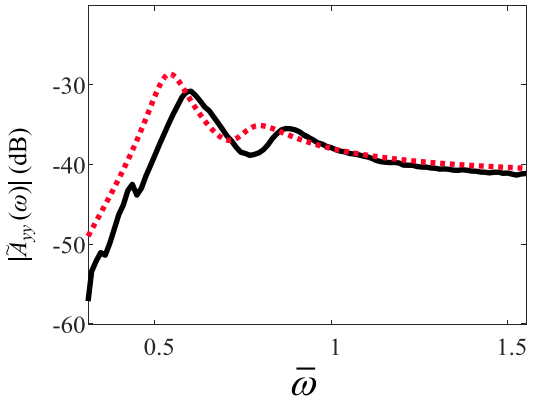

Fig. 16. Comparison of measured and predicted $\left|\tilde{A}_{yy}(\omega)\right|$ spectra for the production isolator (V) with 49 *S* under configuration *T-B*, where $\bar{\omega}$ is the normalized frequency. Key: ▬ – Measurement; ▪▪▪ – Analytical model.

spectra for isolator V under configuration *T-B* under excitation in the *y* direction. Similar to the laboratory isolators it is observed that there is some deviation in the natural frequencies, once again likely due to a change in operating point due to additional preload. Otherwise, satisfactory accuracy is again achieved. Finally, Table 5 compares the bounce stiffness (k_z) values for isolator V obtained from modal experiment configuration *T-A* with measurements made using a non-resonant method under 0.1 mm peak-to-peak sinusoidal displacement excitation and a 60 N preload [2]. Each value is normalized by the k_z value of isolator V at 41 *S*. These show good agreement between methods except for the very high durometer ($S = 68$) materials, where significant deviation between the two methods begins to occur. This may be due to an inadequate value of *E* used (as evident from the discrepancy seen in Fig. 6) or the material non-uniformity associated with such hard samples.

6.3. Identification of production isolators under configuration T-C

The configuration *T-C* of Fig. 2(c) is schematically displayed in Fig. 17. It employs 2 pairs of different production isolators (V and VI), and the properties of each, namely $[K]_O$ and the location of *O* (with eccentricities ε_y and ε_z) are identified, as before, with configuration *T-A*. The analytical model captures the in-plane dynamics of *T-C* in the *y-z* plane assuming physical symmetry; this representation may be reproduced for the *x-z* plan (with $c_x \to 0$) though details are not given here. While the

Table 5
Validation of stiffness k_z values for the production isolator (V) where the modal experimental values are under configuration *T-A* and the non-resonant values are under low-amplitude (0.1 mm peak-to-peak) sinusoidal excitations and 60 N preload in the z-direction. Each value is normalized by the k_z value of isolator V at 41 *S*.

Nominal *S*	$\bar{k}_z$ from modal experiment (N/mm)	$\bar{k}_z$ from non-resonant test (N/mm)
41	1.00	1.17
49	2.11	1.70
59	2.67	2.75
68	8.86	6.70

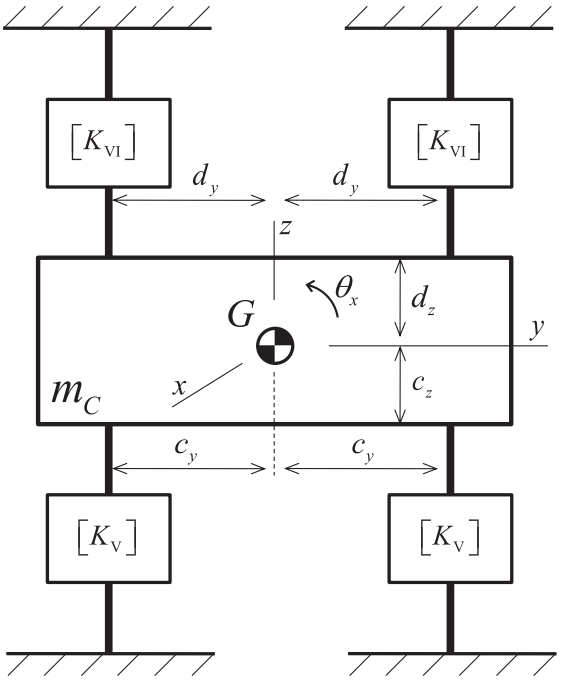

Fig. 17. Analytical 3-DOF model for the isolation system under configuration *T-C* of Fig. 2(c). Here, all of the stiffness properties for production isolators (V and VI) are lumped into two stiffness matrices, namely $[K_V]$ and $[K_{VI}]$, as in Fig. 13. Additionally, m_C is the rigid mass, and c_y, c_z, d_y, and d_z are geometric parameters which locate the isolator hard points from the CG.

production isolator VI (with a hardness of 40 *S* though other details are not provided in this article) is very compliant compared to isolator V, the relative inertia of the vertical plate is much less stable given its vertical orientation. Therefore these isolators (VI) play a significant role in limiting the out-of-plane dynamics. The governing equations for the isolation system in Fig. 17 (from the static equilibrium under a given preload) are found in the same manner as with the other configurations. The system stiffness matrix $[K]_G$ (at the CG) is defined as follows where all the symbols (as defined in Fig. 17) retain their typical meaning,

$$
\begin{aligned}
[K]_G &= \left[T\left(-c_y+\varepsilon_{y,V},-c_z-\varepsilon_{z,V}\right)\right][K_V]\left[T\left(-c_y+\varepsilon_{y,V},-c_z-\varepsilon_{z,V}\right)\right]^T+\left[T\left(c_y+\varepsilon_{y,V},-c_z-\varepsilon_{z,V}\right)\right][K_V]\left[T\left(c_y+\varepsilon_{y,V},-c_z-\varepsilon_{z,V}\right)\right]^T\\
&\quad+\left[T\left(-d_y+\varepsilon_{y,VI},d_z+\varepsilon_{z,VI}\right)\right][K_{VI}]\left[T\left(-d_y+\varepsilon_{y,VI},d_z+\varepsilon_{z,VI}\right)\right]^T+\left[T\left(d_y+\varepsilon_{y,VI},d_z+\varepsilon_{z,VI}\right)\right][K_{VI}]\left[T\left(d_y+\varepsilon_{y,VI},d_z+\varepsilon_{z,VI}\right)\right]^T\\
&= 2\begin{bmatrix} k_{y,V}+k_{y,VI} & 0 & k_{y,V}(c_z+\varepsilon_{z,V})-k_{y,VI}(d_z+\varepsilon_{z,VI}) \\ & k_{z,V}+k_{z,VI} & k_{z,V}\varepsilon_{y,V}+k_{z,VI}\varepsilon_{y,VI} \\ \textit{Symmetric} & & \begin{pmatrix} k_{z,VI}\left(d_z^2+\varepsilon_{z,VI}^2\right)+k_{y,VI}(d_z+\varepsilon_{z,VI})^2+k_{\theta,VI} \\ +k_{z,V}\left(c_z^2+\varepsilon_{z,V}^2\right)+k_{y,V}(c_z+\varepsilon_{z,V})^2+k_{\theta,V} \end{pmatrix} \end{bmatrix}.
\end{aligned}
\tag{27}
$$

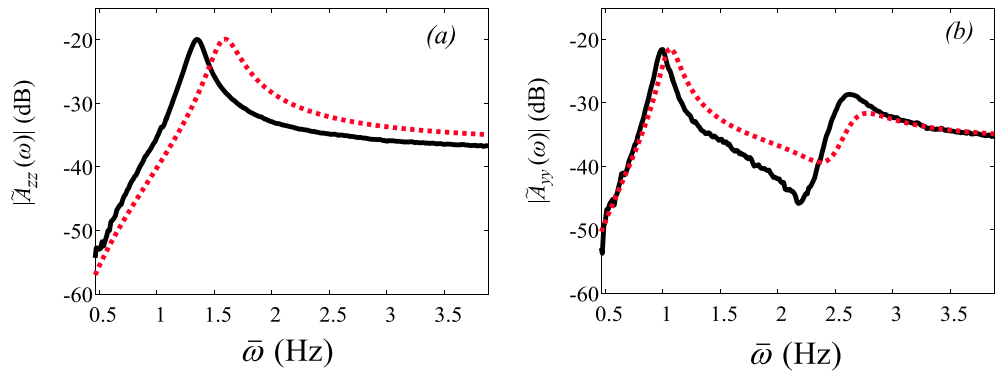

Fig. 18. Comparison of measured and predicted $\left|\tilde{A}(\omega)\right|$ spectra for configuration *T-C* using isolator V of 68 *S* and isolator VI of 40 *S*: (*a*) $\left|\tilde{A}_{zz}(\omega)\right|$, (*b*) $\left|\tilde{A}_{yy}(\omega)\right|$. Key: ▬ – Measurement; ▪▪▪ – Analytical model.

Measured and estimated $\left|\tilde{A}_{zz}(\omega)\right|$ and $\left|\tilde{A}_{yy}(\omega)\right|$ spectra are compared in Fig. 18, showing good accuracy except for a frequency shift which is likely due to out-of-plane dynamics and a significant change in the preload.

7. Conclusion

In this article, rigid body isolation and modal analysis principles are combined to extract the elastic and dissipative properties of vibration isolators. Component-level attributes are related to system-level stiffness and damping matrices, leading to demonstrably unique solutions. Three experimental configurations are employed for modal experiments and system characterization, covering a broad range of isolators in terms of materials as well as laboratory and production level isolators, unlike prior identification methods which focused on one main device under virtually zero mean load. The mass in each experimental configuration is selected to provide appropriate pre-load, stability, and dynamic scaling. In particular, two configurations, with four identical or dissimilar isolators simulating *in situ* isolation application, have yielded the experimental validation. The chief contributions of this article are as follows. First, the proposed identification procedure highlights the role of the elastic center as an intrinsic component-level property where the diagonal stiffness matrix becomes diagonal. Only then can the system stiffness be properly formulated, since off-diagonal stiffness terms depend on the hard-point location; this issue seems to have been largely ignored in the prior literature. The proposed procedure also facilitates the development of analytical models in the context of a physically symmetric problem (of dimension 3), which simplifies the identification process while guiding experimental and computational studies. Second, the system stiffness matrices (including the off-diagonal terms) of several elastomeric mounts have been developed, computationally verified and experimentally validated. Third, alternate damping formulations are investigated, including mode-independent loss factor, Rayleigh viscous damping, and—more broadly—proportional damping matrices (of dimension 3) for each isolator. The viscous damping matrices seem to yield the best frequency response curves when addressing coupled rocking-shear modes where the frequency spacing between resonances and anti-resonances is rather narrow.

Finally, the identification procedure of this article (based on a combination of lumped-parameter analytical and finite element models that are well supported by modal experiments) provide improved physical insight into the underlying behavior of elastomeric interfacial elements by highlighting the role of the elastic center, structural or viscous damping models, and identifying the correlation between surface hardness and Young's Modulus in the context of dynamic loading. The main limitations of the proposed process are due to the assumptions made, namely the linear time-invariant system theory, proportional damping, homogenous materials and the like; such necessary assumptions have also been made by prior researchers.

Acknowledgements

The authors would like to thank the member organizations of the Smart Vehicles Concepts Center (www.SmartVehicleCenter.org), the National Science Foundation Industry University Cooperative Research Centers program (www.nsf.gov/iip/iucrc) and the Ford Motor Company (with contributions from Y. Zhang, L. Liang, Y. Miao, and D. Prajapati) for supporting this work.

Appendix A: List of symbols

A	accelerance
a, b, c, d	geometric parameters for experimental configurations
C	viscous damping matrix
D	diameter
E	Young's modulus
F	generalized force
G	center of gravity location
h	amplitude coefficient
I	identity matrix
J	mass moment of inertia
K	stiffness matrix
k	spring constant
L	length
M	mass matrix
m	mass
n	modal index
O	elastic center location
P	hard point location

(*continued on next page*)

Appendix A (*continued*)

Q	reference point
q	generalized displacement
S	Shore A durometer
T	transformation matrix
t	time
u	translational displacements
x, y, z	cartesian coordinates
β	proportionality constant for Rayleigh damping
γ	empirical coefficient
ε	elastic center coordinate
ζ	damping ratio
η	loss factor
θ	rotational displacements
Λ	eigenvalue matrix
λ	empirical coefficient
ν	Poisson's ratio
ξ	modal displacement
ρ	density
ϕ	eigenvector, modal matrix
ω	circular frequency, rad/s
Subscripts	
I, II, III, IV, V, VI	isolator designation
o	operating point
r	reference value
s	static
Superscripts	
$-$	normalized value
$\sim$	complex valued
^	estimated/conditioned value
Abbreviations	
CG	center of gravity
diag	diagonal matrix
DOF	degrees of freedom
MAC	modal assurance criterion
Designations	
I, II, III, IV, V, VI	isolators used in the study
T-A, T-B, T-C	test (modal) experiment configurations

References

[1] J. Gillibert, M. Brieu, J. Diani, Anisotropy of direction-based constitutive models for rubber-like materials, Int. J. Solids Struct. 47 (2010) 640–646.
[2] MTS, Model 831.50 x 1000 Hz elastomer test system features high frequency test capability. https://mts.com/ucm/groups/public/documents/library/dev_002249.pdf, 2004 (accessed 20 December 2017).
[3] S. Noll, B. Joodi, J. Dreyer, R. Singh, Volumetric and dynamic performance considerations of elastomeric components, SAE Int. J. Mater. Manf. 8 (3) (2015) 953–959.
[4] S. Noll, J.T. Dreyer, R. Singh, Identification of dynamic stiffness matrices of elastomeric joints using direct and inverse methods, Mech. Syst. Signal Process. 39 (2013) 227–244.
[5] B. Joodi, S. Noll, J. Dreyer, R. Singh, Comparative assessment of frequency dependent joint properties using direct and inverse identification methods, SAE Int. J. Mater. Manuf. 8 (3) (2015) 960–968.
[6] L. Fredette, J.T. Dreyer, T.E. Rook, R. Singh, Harmonic amplitude dependent dynamic stiffness of hydraulic bushings: alternate nonlinear models and experimental validation, Mech. Syst. Signal Process. 75 (2016) 589–606.
[7] J.Y. Yoon, R. Singh, Indirect measurement of dynamic force transmitted by a nonlinear hydraulic mount under sinusoidal excitation with focus on super-harmonics, J. Sound Vib. 329 (2010) 5249–5272.
[8] L. Kari, Dynamic transfer stiffness measurements of vibration isolators in the audible frequency range, Noise Control Eng. J. 49 (2001) 88–102.
[9] D.J. Thompson, W.J. Van, J.W. Verheij Vliet, Developments of the indirect method for measuring the high frequency dynamic stiffness of resilient elements, J. Sound Vib. 213 (1) (1998) 169–188.
[10] T.R. Lin, N.H. Farag, J. Pan, Evaluation of frequency dependent rubber mount stiffness and damping by impact test, Appl. Acoust. 66 (2005) 829–844.
[11] L.E. Ooi, Z.M. Ripin, Dynamic stiffness and loss factor measurement of engine rubber mount by impact test, Mater. Des. 32 (2011) 1880–1887.
[12] S. Kim, R. Singh, Multi-dimensional characterization of vibration isolators over a wide range of frequencies, J. Sound Vib. 245 (5) (2001) 877–913.

[13] J.W.R. Meggitt, A.S. Elliott, A.T. Moorhouse, H.K. Lai, In situ determination of dynamic stiffness for resilient elements, Proc. IMechE PartC: J. Mech. Eng. Sci. 230 (6) (2016) 986–993.
[14] J.P. Den Hartog, Mechanical Vibrations, fourth ed., McGraw-Hill, New York, 1956.
[15] T. Jeong, R. Singh, Analytical methods of decoupling the automotive engine torque roll axis, J. Sound Vib. 234 (1) (2000) 85–114.
[16] A.N. Gent, On the relation between indentation hardness and Young's modulus, Rubber Chem. Technol. 31 (4) (1958) 896–906.
[17] J.P. De Clerck, Using singular value decomposition to compare correlated modal vectors, Proc. SPIE Int. Soc. Opt. Eng. 2 (1998) 1022–1029.
[18] British Standard 903 (1950, 1957), Methods of testing vulcanised rubber, Part 19 (1950) and Part A7 (1957).
[19] W.T. Thomson, Theory of Vibration with Applications, fourth ed., Prentice-Hall, New Jersey, 1993.
[20] M. Rao, S. Gruenberg, D. Griffiths, Measurement of dynamic parameters of automotive exhaust hangers, SAE Technical Paper 2001-01-1446, (2001).
[21] L. Fredette, R. Singh, High frequency, multi-axis dynamic stiffness analysis of a fractionally damped elastomeric isolator using continuous system theory, J. Sound Vib. 389 (2017) 468–483.
[22] L. Yu, S. Liu, L. Ye, G. Huang, Y. Xu, The dynamic characteristics of silicone rubber isolator, J. Wuhan Univ. Technol. Mater. Sci. Ed. 27 (1) (2012) 130–133.